# Thickness-Dependent Hydrophobicity of Epitaxial Graphene

Martin Munz,[†] Cristina E. Giusca,[†] Rachael L. Myers-Ward,[‡] D. Kurt Gaskill,[‡] and Olga Kazakova*,[†]

[†]National Physical Laboratory, Hampton Road, Teddington TW11 0LW, U.K. and [‡]U.S. Naval Research Laboratory, Washington, D.C. 20375 United States

ABSTRACT This article addresses the much debated question whether the degree of hydrophobicity of single-layer graphene (1LG) is different from that of double-layer graphene (2LG). Knowledge of the water affinity of graphene and its spatial variations is critically important as it can affect the graphene properties as well as the performance of graphene devices exposed to humidity. By employing chemical force microscopy with a probe rendered hydrophobic by functionalization with octadecyl-trichlorosilane (OTS), the adhesion force between the probe and epitaxial graphene on SiC has been measured in deionized water. Owing to the hydrophobic attraction, a larger adhesion force was measured on 2LG Bernal-stacked domains of graphene surfaces, thus showing that 2LG is more hydrophobic than 1LG. Identification of 1LG and 2LG domains was achieved through Kelvin probe force microscopy and Raman spectral mapping. Approximate values of the adhesion force per OTS molecule have been calculated through contact area analysis. Furthermore, the contrast of friction force images measured in contact mode was reversed to the 1LG/2LG adhesion contrast, and its origin was discussed in terms of the likely water depletion over hydrophobic domains as well as deformation in the contact area between the atomic force microscope tip and 1LG.
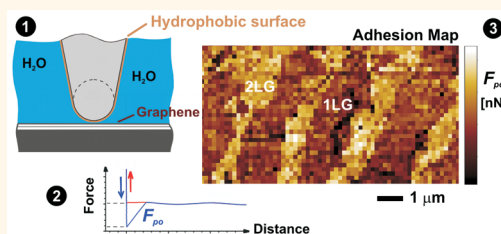
KEYWORDS: epitaxial graphene · hydrophobic/hydrophilic · chemical force microscopy · lateral force microscopy · Kelvin probe force microscopy · adhesion · friction

Since its first successful isolation *via* the mechanical exfoliation method,[1,2] graphene, a single sheet of sp^2-hybridized carbon atoms which may be characterized as a single sheet of graphite, has attracted an enormous amount of interest, owing to its outstanding electrical, optical, and mechanical properties.[3] Major challenges being addressed are the large-scale production of graphene[2,4] as well as control of its properties under a variety of environmental conditions.[5,6]

The properties of graphene, a two-dimensional (2D) material, are highly susceptible to surface interactions, thus enabling chemical sensing applications with high sensitivity. Adsorption-induced doping can alter the characteristics of a graphene device and make it susceptible to variations of the environmental conditions.[2,7] In particular, this is the case for operation under ambient conditions, where water molecules or other foreign species[8–10] can adsorb from air.

The adsorption of water molecules on a graphene surface is closely related to its hydrophobicity. A clean, multilayer graphene (MLG) surface may be expected to approach the properties of graphite, as the number of stacked graphene layers goes to infinity ($N \rightarrow \infty$) and, *a priori*, is widely considered nonpolar and thus hydrophobic (see ref 10 and references therein). However, in the limit of single-layer graphene (1LG) or double-layer graphene (2LG), property variations may occur, for example, due to different levels of doping depending on the graphene thickness as this gives rise to work function variations[11,12] which, in turn, may impact the adsorption of molecules and the wetting behavior. Several experimental[13–15] and theoretical studies[16,17] indicated variations in the wetting behavior of 1LG, 2LG, and MLG surfaces.

Since variations in water wettability are likely to affect graphene properties, ranging from adhesion and friction[18] to electrical charge doping[19] and permeation,[20] it is important to develop a thorough understanding of its wetting behavior. Frequently, experimental studies rely on measurements of the water contact angle (WCA) as it provides a measure for the degree of hydrophobicity of graphene surfaces.[10,13–16] However, such WCA measurements are typically performed on a macroscopic length scale that averages over a large number of graphene domains. To account for the micron-scale morphology

of epitaxial graphene samples, microscopic or meso-scopic techniques are needed. Chemical mapping techniques, such as Raman spectral mapping can be highly useful in identifying different domains of a complex graphene morphology;[21−23] however, com-plementary techniques are required to measure quan-tities directly related to the wetting behavior. Chemical force microscopy (CFM), a variant of atomic force microscopy (AFM), uses chemically functionalized probes to measure either force−distance curves or the lateral forces (lateral force microscopy, LFM) occur-ring between the scanning tip and the surface under investigation.[24−29] Employing CFM, both the adhesion and friction properties of graphene were studied previously.[30−32]

It should be noted that when measured *in air*, specific force interactions can be obscured by the relatively large capillary force resulting from the con-densation of water in the narrow gap between AFM tip and the sample surface, including contributions re-lated to the capillary pressure and to the surface tension.[33,34] At nonzero levels of relative humidity (RH), the capillary force tends to be the major force component[30,34] and is larger on hydrophilic areas where the water contact angle is smaller.[31,33,35,36] On hydrophilic surfaces, the measured pull-off force largely increases with the RH, although non-monotonic variations may occur in the regime of high RH levels above ∼70−80%, depending on the particulars of the AFM tip geometry.[33,34,36] In contrast to hydrophilic surfaces, a vanishing RH dependence is typically ob-served on hydrophobic surfaces.[33,36,37] Thus, in the presence of humid air, capillary forces play a vital role if the surface is hydrophilic and the measured pull-off force, F_{po}, tends to be larger (Figure 1a).

In the case of the AFM tip and sample immersed into *a liquid medium*, the measured adhesion force critically depends on the polarity of the liquid. The adhesion force between hydrophilic surfaces was found to be larger for a hydrophobic liquid.[25,38] Conversely, the adhesion force measured between two hydrophobic surfaces tends to be larger if they are immersed into a polar liquid, such as water. The latter phenomenon is referred to as hydrophobic attraction[39] and has been addressed by several reports[25,38,40] considering the effect of the liquid medium polarity on the measured pull-off force, F_{po}. Essentially, such studies suggest that in a polar liquid F_{po} scales with the degree of hydro-phobicity (Figure 1b). For a qualitative discussion, there is no need to specify whether or not the relationship is linear, although a linear approximation can be assumed if a small hydrophobicity range is considered.

We utilize the hydrophobic attraction for analytical purposes, that is, to discern between hydrophilic and hydrophobic surface areas through adhesion force measurements (Figure 1b), notwithstanding some controversies[39,41−43] concerning the origin of the hydrophobic attraction. We have chosen water as a polar liquid to facilitate comparatively large adhesion forces between hydrophobic AFM tips and domains of epitaxial graphene with different degrees of hydro-phobicity.

In this article, the results of CFM measurements on epitaxial graphene are reported with a focus on the adhesion force variations between 1LG and 2LG. AFM tips with a hydrophobic surface functionalization have been used to map spatial variations in the hydro-phobicitiy of epitaxial graphene surfaces synthesized by graphitization of a SiC single crystal. The surface of Si AFM tips was chemically functionalized, using a CH_3-terminated monolayer of octadecyltrichlorosilane (OTS, $CH_3(CH_2)_{17}SiCl_3$), and the adhesion mapping was carried out in deionized water. Using test samples with a hydrophobic/hydrophilic pattern, the approach rely-ing on hydrophobic attraction has been demonstrated. Its application to the adhesion contrast occurring on 1LG and 2LG domains indicates that 1LG is less hydro-phobic than 2LG. Furthermore, this finding has been analyzed in conjunction with subsequent friction force measurements in water and is compared to results of adhesion force measurements conducted under ambient conditions.

RESULTS AND DISCUSSION

Adhesion and Surface Potential of Epitaxial Graphene under Ambient Conditions. Initially, we considered the case of graphene under ambient conditions where capillary condensation occurs. Using Kelvin probe force micro-scopy (KPFM) mode, we imaged the surface potential of the graphene surface and its spatial variations. The KPFM signal is helpful in quantitatively characterizing the local graphene layer number and identifying 1LG and 2LG domains.[11,12,15] The height, adhesion, and KPFM images of the graphene surface are given in Figure 2.
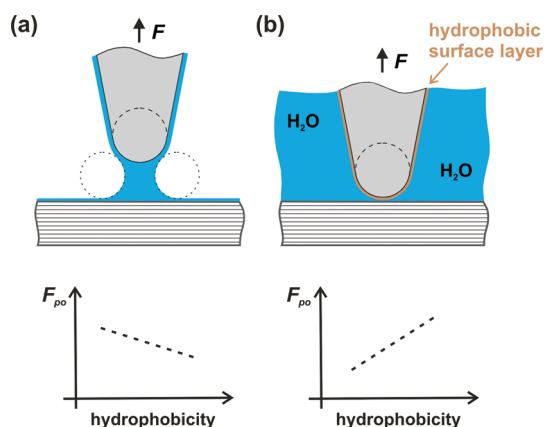

Figure 1. Schematic of AFM adhesion force measurements under different environmental conditions and related varia-tions of the pull-off force, F_{po}, with the degree of hydro-phobicity of the surface under investigation. (a) In humid air, using a plain Si tip. (b) In water, using an AFM tip with a hydrophobic surface functionalization.
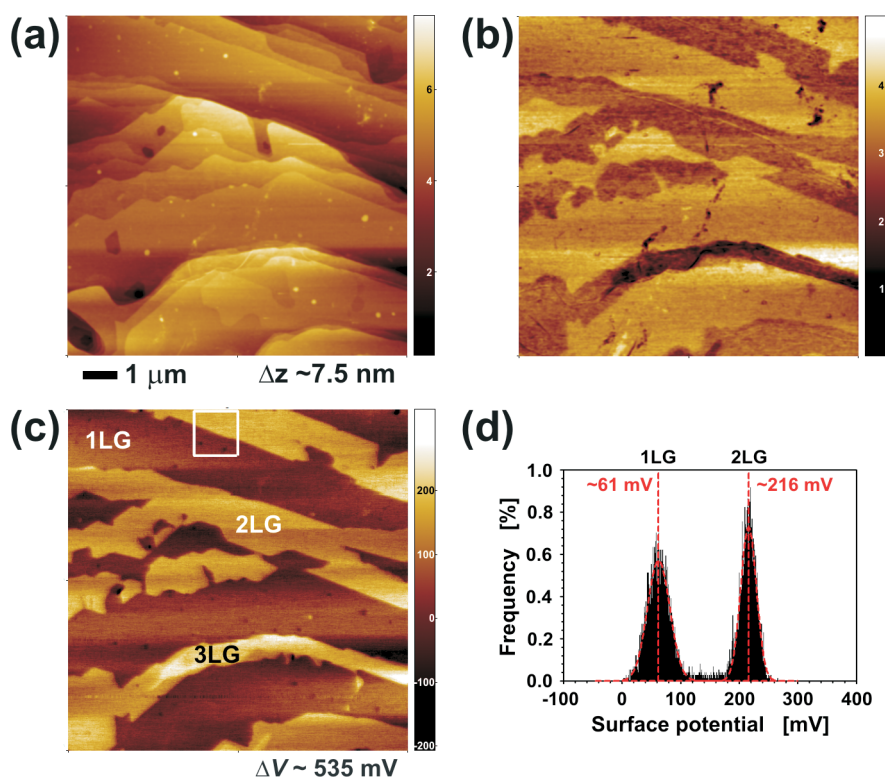
Figure 2. Epitaxial graphene surface imaged in air (RH ~ 40%), using a hydrophilic AFM probe. (a) Topography, (b) adhesion measured in PeakForce mode, and (c) surface potential measured in FM-KPFM mode. (d) Histogram associated with the area enclosed by the white square in (c). In (b), the adhesion force range is ~5.1 nN. The scan width in (a–c) is 10 μm.

The surface potential image (Figure 2c) shows a strong contrast between 1LG and 2LG domains, due to the relative difference in their work functions. This is furthermore highlighted by the histogram (Figure 2d) associated with the area marked with the white square in Figure 2c, displaying a bimodal surface potential distribution corresponding to 1LG and 2LG. To determine the surface potential values associated with 1LG and 2LG, peak deconvolution was carried out using Gaussian shape components, and layer thickness was designated in accordance with the domain contrast in the surface potential image.

The surface potential values obtained for 1LG and 2LG (~61 and 216 mV, respectively) have been used to determine the corresponding work function values, using $eU_{CPD} = \Phi_{tip} - \Phi_{surface}$, where U_{CPD} is the contact potential difference (surface potential) measured by KPFM.[12] The work function of the KPFM tip (4.52 ± 0.02 eV) was determined by calibration against a reference gold sample, the work function of which had been measured using ultraviolet photoelectron spectroscopy. With the KPFM tip value, the work function values of 4.47 ± 0.02 and 4.32 ± 0.02 eV were obtained for 1LG and 2LG, respectively. The value obtained for 1LG is consistent with previous KPFM studies in ambient, reporting a work function value of ~4.5 eV for graphene.[44−46] The assignment of the observed domains to 1LG and 2LG is further corroborated by Raman maps of this sample, as detailed in Figure S1

(Supporting Information), showing a morphology similar to that observed by KPFM.

Furthermore, the adhesion image in Figure 2b shows larger pull-off forces on the domains where a larger work function was measured (i.e., on the 1LG domains). As the measurements were taken in humid air (RH ~ 40%) and the tip was hydrophilic (doped Si tip with no further surface functionalization), capillary condensation of water in the narrow gap between the AFM tip and the sample surface occurred. Following the rationale depicted in Figure 1a, under these conditions, a larger pull-off force is observed on areas which are less hydrophobic. Thus, the images in Figure 2b indicate that 1LG domains are less hydrophobic than 2LG domains.

Additionally, a thin curved domain across the lower half of the images in Figure 2b,c can be seen, which is characterized by lower adhesion and higher surface potential values compared to those in 1LG and 2LG domains. It can be identified as a 3LG domain that appears even more hydrophobic than the 2LG domains.

Adhesion Mapping of Test Samples in Water. To demonstrate the effect of the tip surface chemistry on the tip–sample adhesion force, two test samples were measured in DI water using plain as well as OTS-functionalized tips. OTS binds to silica surfaces via the silane group and exhibits a terminal CH_3 group at its free end. The structural–mechanical properties of OTS monolayers have been described in several reports.[37,42,47,48] For an OTS monolayer on SiO_2, the WCA is ~110°.[16,49]
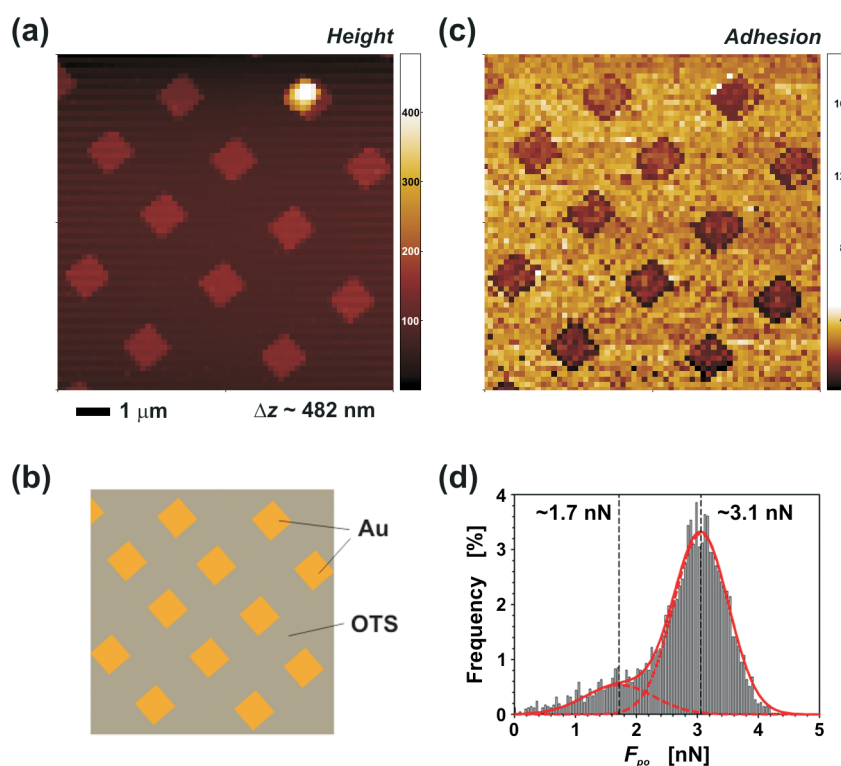
Figure 3. Results of force mapping of TS1 (with OTS functionalization), using an OTS-functionalized probe. (a) Height map, (b) schematic of the chemical pattern, (c) adhesion map, and (d) histogram of the adhesion map with the Gaussian fits to the peaks indicated by red lines. In (c), the adhesion force range is ~18.8 nN. In (a,c), the scan width is 10 μm, and the pixel number is 64 × 64. Cantilever spring constant is ~184 pN/nm, and resonance frequency in air is ~20.92 kHz.

Furthermore, a typical value for the surface free energy of CH$_3$-terminated monolayers with water is $\gamma_{sl} \sim 52$ mJ/m^2.[26,50]

Both test samples consisted of arrays of gold squares on top of a silicon wafer. By making use of the silica surface layer of the silicon wafer, one of the test samples was functionalized with OTS. As a result, the hydrophilic gold squares are surrounded by a hydrophobic area terminated with CH$_3$ groups of the OTS molecules (Figure 3b). In the following, this sample is referred to as test sample TS1. Contrary to the first control sample, the second one was treated in a UV/ozone cleaner, but no further functionalization was applied. That is, its surface remained hydrophilic throughout, unless adsorption of hydrocarbons from the air occurred. This sample is referred to as test sample TS2. Force mapping results of test sample TS1 are given in Figure 3 and of sample TS2 in Figure S2 (Supporting Information). In both cases, an OTS-functionalized probe was used. As can be seen from the adhesion map shown in Figure 3c, a larger adhesion force was measured on the area between the gold squares, that is, the hydrophobic area terminated with CH$_3$ groups. The histogram related to the force map of Figure 3c is given in Figure 3d. It encompasses a distinct peak with its center at ~3.1 nN and a shoulder on the low force side, which indicates the presence of a second peak with the center around ~1.7 nN. The former is related to the OTS-functionalized

area, which is the larger fraction of the total area, and the latter is related to the gold squares where the adhesion force was lower. As the maps of Figure 3 show ~12.5 squares, the relative area covered by the squares is 12.5 μm^2/100 μm$^2 \sim$ 12.5%.

Thus, for the present condition of force mapping in DI water, a larger adhesion force was measured for the OTS—OTS contact. This finding is consistent with Figure 1b, which illustrates that in water the adhesion force is larger if both surfaces are hydrophobic.

Adhesion Mapping of Epitaxial Graphene in Water. Similarly to the test samples, the surface of a graphene sample grown epitaxially on SiC was analyzed in DI water using OTS-functionalized probes. An adhesion map and typical force—distance curves are given in Figure 4a. The pull-off peaks occur upon retraction (blue curves), and their height is a measure for the tip—sample adhesion force. Each pixel of the adhesion map gives the absolute value of the peak height (attractive forces are negative). Clearly, the adhesion map shows bright lamellae, where the pull-off force is larger, alternating with darker lamellae. The associated histogram (Figure 4b) shows a bimodal distribution with peaks around ~4.6 ± 1.4 and ~7.6 ± 1.6 nN, where the uncertainty levels are given by FWHM/2. Following the above rationale (Figures 1, 3, and 4), areas where larger adhesion forces between the surface and the hydrophobic tip occur are more hydrophobic than areas where the adhesion force
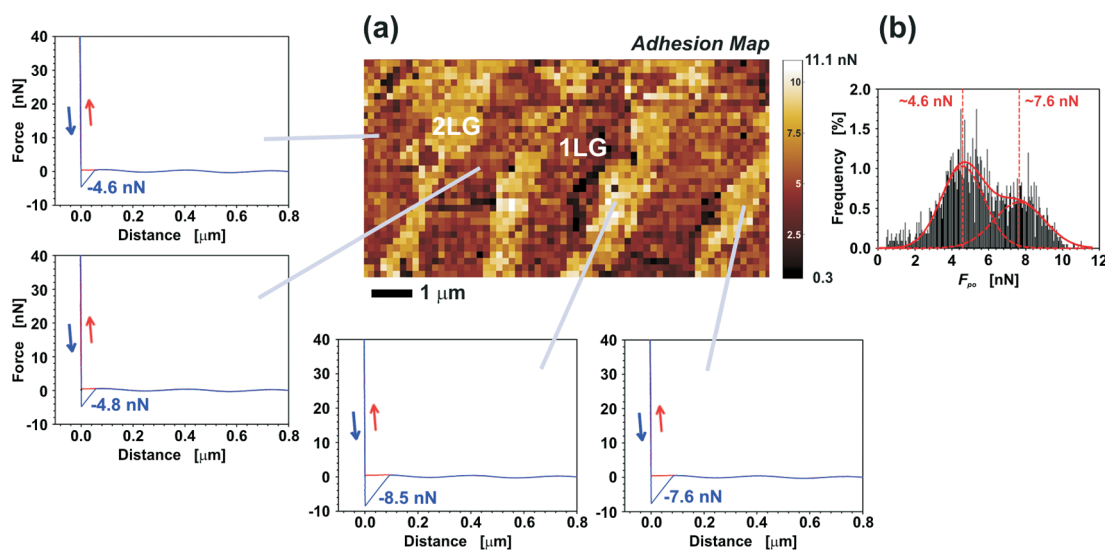
Figure 4. (a) Adhesion map of the graphene surface in DI water and typical force−distance curves measured at the indicated locations. The force range of the adhesion map is ∼10.8 nN. Force−distance curves measured upon approach and retraction are shown in red and blue, respectively. (b) Histogram associated with the adhesion map shows peaks at ∼4.6 and ∼7.6 nN. The FWHM values of the Gaussian peaks are ∼2.7 and 3.2 nN, respectively.

is lower. Furthermore, from Raman and KPFM mapping, it is known that such lamella-shaped domains are typically 2LG, whereas the areas in between are 1LG (Figure S1 in the Supporting Information and Figure 2c). Taken together with the adhesion contrast, this implies that 2LG is more hydrophobic than 1LG.

An adhesion map with a similar contrast but a less regular pattern of domains is given in Figure 5a. The associated histogram (Figure 5b) shows a broad distribution, which has been deconvoluted by analyzing the histograms (Figure S4 in the Supporting Information) of both dark and bright adhesion map areas. The analysis yields two Gaussian peaks at ∼1.9 ± 0.4 and 2.3 ± 0.3 nN, and the total distribution relating to the entire map can be approximated by a linear combination of these Gaussians.

It should be noted that the measured adhesion force is the total force needed to disrupt the "bonds" between the OTS-functionalized AFM tip and the graphene surface. The measured adhesion force is due to the strength of attraction between a number of OTS molecules interacting across the tip−sample contact with the graphene surface, governed by the finite size of the AFM tip. In the following, the interaction with a single OTS molecule is referred to as a "bond", even if no actual covalent bond is formed. *A priori*, it is unknown whether the measured adhesion force corresponds to a single or several "bonds". An estimation of the adhesion force between a single OTS molecule and 1LG or 2LG is given below (see the section, Estimation of the Adhesion Force between 1LG/2LG and a Single OTS Molecule).

Subsequently to the force mapping, the area has been imaged in contact mode, which affords a larger number of pixels and thus a higher pixel resolution

(here, 256 pixels per 1.76 μm). It is interesting to note that the pixel resolution of ∼6.9 nm/pixel (1760 nm/256 pixels) is similar to the determined tip radius of ∼6.3 nm (see section, Estimation of the Adhesion Force between 1LG/2LG and a Single OTS Molecule) and the typical tip radius of ∼8 nm as specified by the manufacturer. In the small deformation regime, the tip radius is an upper bound for the tip−sample contact radius, which is a measure for the lateral spatial resolution. The resulting topography and lateral force images are given in Figure 5c,d, respectively. Regions associated with 2LG display an increased adhesion force (bright areas in Figure 5a) and correspondingly a reduced lateral/friction force (dark area in Figure 5d). Compared to 2LG, 1LG domains show lower adhesion and increased friction force, respectively (see also Figure S5 in the Supporting Information). Notably, from the step edges displayed in the topography image (Figure 5c), it is impossible to differentiate graphene domain edges from SiC terrace edges. It is well-known that step edges can also occur within a uniform graphene domain, due to the growth process consuming carbon atoms of the SiC substrate and thus causing height variations of its surface.[11]

In general, the graphene samples presented here were largely composed of 1LG and 2LG domains. The KPFM and adhesion images of Figure 2 show only a small 3LG domain area (less than ∼5% of the scan area), and from the Raman maps measured at several locations across the sample surface, there was no evidence for a significant fraction of 3LG (less than ∼10% of the total area) or MLG domains. The lateral resolution of the Raman maps was ∼400 nm.

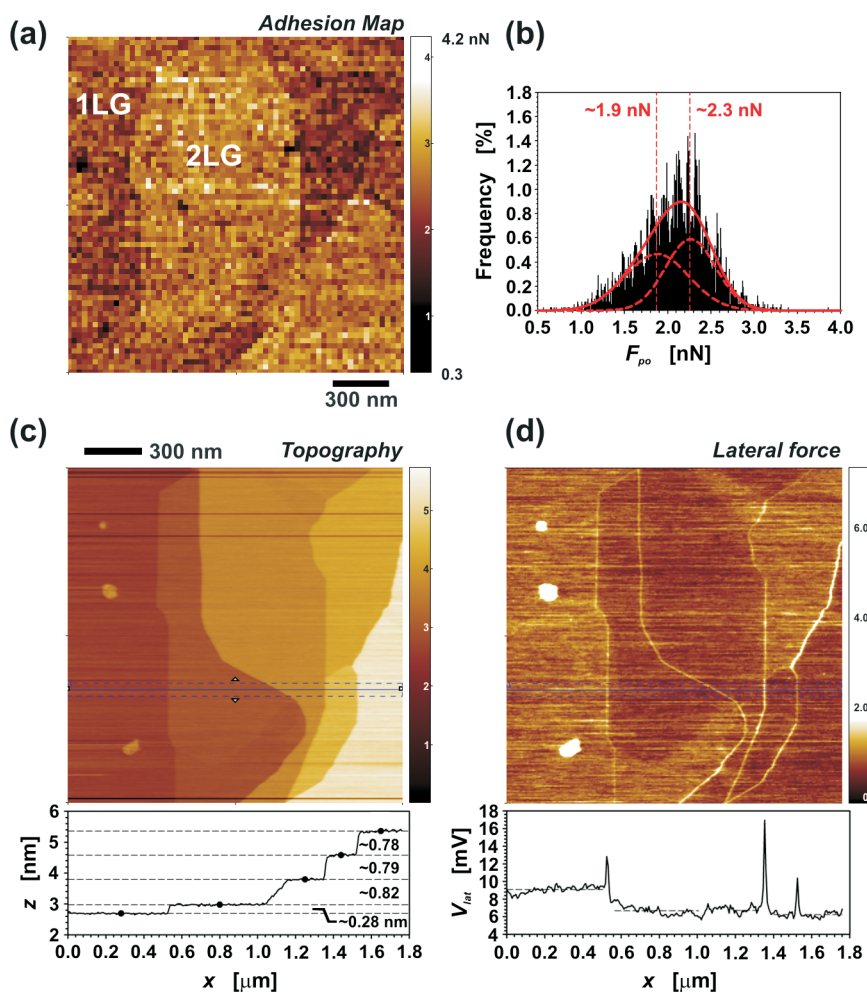A correlation between adhesion and friction forces is described by the Bowden-Tabor adhesion model for

Figure 5. Adhesion and friction force measurements on graphene, using an OTS-functionalized hydrophobic tip in water. (a) Adhesion map, 64×64 pixels, force range $\sim$3.9 nN. (b) Histogram associated with the adhesion map is composed of peaks around $\sim$1.9 and 2.3 nN (further analysis of the data is shown in Figure S5 in the Supporting Information). (c) Topography image measured in contact mode and a cross-sectional profile (averaged over 11 consecutive lines within the horizontal rectangle marked with a dashed blue line). (d) Lateral force image and a cross-sectional profile. In (a, c, and d), the scan width is 1.76 μm.

interfacial friction. It states that the friction force scales in a linear manner with the true contact area, A, and with the shear strength, τ, as a constant factor.[48,51] While an AFM tip is sliding across a surface, continuous formation and rupture of "bonds" occur, causing a friction force. In addition, a load-dependent contribution, $F_p(L)$, may occur where the sliding tip deforms a soft surface layer, such as an OTS monolayer. This second contribution is referred to as ploughing force,[48] and the total friction force can be written as $F_f = \tau A + F_p$. Thus, changes in F_f may result from variations in τ, A, and F_p. If the shear strength, τ, scales with the adhesion force measured (Figure 5a), then τ should be lower on 1LG. However, this variation can be counterbalanced or even overcompensated by an increase in A or F_p.

Notably, the observation of an increased friction force on 1LG (Figure 5d) is consistent with reports of friction force measurements both in ultrahigh vacuum and under ambient conditions. For graphene as well as other 2D materials, including MoS_2, $NbSe_2$, and hexagonal

boron nitride, Lee et al.[18] found that the friction force increased as the number of layers decreased. The largest force was measured for single-layer domains and attributed to out-of-plane puckering, which causes an increase in the tip–sample contact area, A. In the case of graphene, such out-of-plane elastic deformation should be more pronounced for 1LG domains due to their low bending stiffness.[18]

In addition, if the ploughing term, F_p, encompasses the force needed to move the AFM tip through interfacial layers of water molecules, then variations in friction force may also depend on local variations in water density or in the ordering of water molecules nearby the surface. In particular, on hydrophobic areas, lower forces may be needed to displace water molecules because hydrophobicity tends to be accompanied by a low-density depletion layer, which, in turn, allows water slipping.[43,52,53] Thus, the observed friction force contrast (Figure 5d) may also result from spatial variations of the water depletion layer.

Irrespective of the causes of the friction force contrast, Figure 5 exemplifies that LFM can be very useful in locally differentiating graphene domains from each other. Hence, it is highly recommended to measure both the adhesion and the friction forces, using the same AFM tip, to enable correlative analysis and to develop a better understanding of the surface morphology and related friction force variations.

Estimation of the Adhesion Force between 1LG/2LG and a Single OTS Molecule. Since the measured adhesion force scales with the AFM tip size and thus the number of OTS−graphene "bonds" across the tip−sample contact, it is difficult to compare measurements made using different AFM probes. Normalization can be achieved by calculating the adhesion force per OTS molecule if the tip size is known. The adhesion force per OTS molecule in the contact can be estimated by considering the contact area at the pull-off point. The Johnson−Kendall−Roberts (JKR) theory for mechanical contacts between elastic solids accounts for both compressive and adhesive forces.[54] At the instability point where the AFM tip is pulled off from the surface, the contact radius is given by

$$a_{po}^3 = \frac{3}{2}\frac{\pi w R^2}{K} \qquad (1)$$

where K is the reduced modulus of the tip−sample contact, R is the radius of curvature of the tip apex, and w is the work of adhesion per unit area. The relationship between the latter and the force, F_{po}, measured at the pull-off point is

$$F_{po} = -\frac{3}{2}\pi w R \qquad (2)$$

Importantly, w is related to the surface free energies of the sample−liquid and the tip−liquid interfaces, that is, γ_{sl} and γ_{tl}. Here, the liquid is deionized water. With the free energy γ_{ts} of the tip−sample interface, w can be written as

$$w = \gamma_{sl} + \gamma_{tl} - \gamma_{ts} \qquad (3)$$

The reduced modulus is related to the Young's moduli, E_t and E_s, of the tip and sample materials:

$$K = \frac{4}{3}\left[\frac{1-v_1^2}{E_1} + \frac{1-v_2^2}{E_2}\right]^{-1} \qquad (4)$$

where v_t and v_s denote the respective Poisson ratios.

An implication of eq 3 is that for two mating surfaces with identical chemistry, the work of adhesion is $w = \gamma_{sl} + \gamma_{tl} = 2\gamma$, as the interfacial free energy is vanishing. Such a configuration occurred when mapping the OTS-functionalized area of the test sample TS1 with an OTS-functionalized AFM tip (Figure 3). As can be seen from the histogram in Figure 3d, the mean pull-off force measured on OTS, that is, the area between the gold squares, was ∼3.1 ± 0.6 nN.
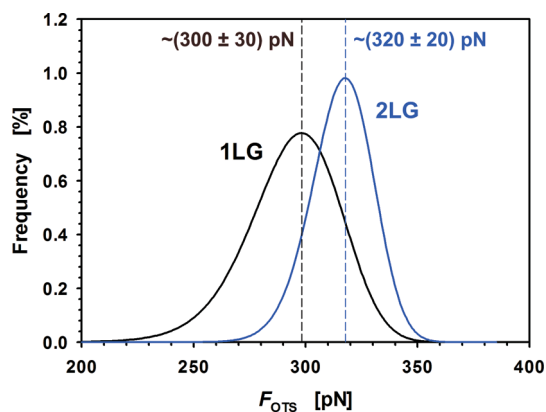

Figure 6. Histograms of the pull-off force, F_{OTS}, per OTS molecule, calculated by applying eqs 4 and 6 to the deconvoluted peaks of the histogram given in Figure 5b. The black and blue curves show the distributions related to 1LG and 2LG, respectively.

With $\gamma_{sl} \sim 52$ mJ/m² for the OTS−water interface,[26,50] an approximate value of ∼6.3 ± 1.2 nm is obtained for the tip radius, R, which can be written as R = $F_{po}/(3\pi\gamma)$ if $w = 2\gamma$ (see eq 2). This tip radius is in reasonable agreement with a typical value of ∼8 nm specified by the manufacturer.

Moreover, the JKR model allows estimation of the average adhesion force between a single OTS molecule on the tip surface and 1LG or 2LG. Using eqs 1, 2, and 4, the contact radius and thus the contact area, $A_{po} = \pi a_{po}^2$, at the pull-off can be calculated if the elastic properties of the tip and sample materials as well as the tip radius, R, are known. With a cross-sectional area, A_{OTS}, per OTS molecule, the number of OTS molecules in the tip−sample contact is $n_{OTS} = A_{po}/A_{OTS}$ and, thus the pull-off force per OTS molecule is given by

$$F_{OTS} = \frac{F_{po}}{n_{OTS}} = \frac{A_{OTS}}{A_{po}}F_{po} \qquad (5)$$

A typical value of A_{OTS} is 0.43 ± 0.07 nm².[55]

With eqs 1 and 2, the contact area can be expressed in terms of F_{po}, that is, $A_{po} = \pi((R/K)|F_{po}|)^{2/3}$, and the pull-off force per OTS molecule written as

$$F_{OTS} = \frac{A_{OTS}}{\pi}\left(\frac{K^2}{R^2}|F_{po}|\right)^{1/3} \qquad (6)$$

For a tip radius of $R \sim 6.3$ nm (see above), eqs 4 and 6 give an F_{OTS} value of ∼300 ± 30 pN for 1LG and ∼320 ± 20 pN for 2LG. In Figure 6, the distributions resulting from the fit curves of Figure 5b are shown, after conversion of the F_{po} values into F_{OTS} values. Comparison of the F_{OTS} values to the total adhesion force, F_{po}, measured (Figure 5b) suggests that about 6.4 (1LG) to 7.2 (2LG) OTS−graphene "bonds" were ruptured when detaching the AFM tip from the respective graphene domains.

The given error margins resulted from the width at half-maximum of the histograms after conversion of

$|F_{po}|$ to F_{OTS} values (Figure 6). The assumed values of Young's modulus and Poisson's ratio for the OTS-functionalized Si AFM tip were 10 GPa and 0.33, respectively.[50] For graphene, the respective values of 1000 GPa and 0.15 can be assumed.[56,57] It should be noted that the calculated values for the adhesion force between a single OTS molecule and the graphene surface are approximate, as the tip radius, R, and the area per OTS molecule, A_{OTS}, are associated with considerable uncertainties. For $R \sim 6.3$ nm, the uncertainty associated with variations of adhesion force across the OTS–OTS contact (Figure 3c,d) is $\Delta R \sim \pm 1.2$ nm. As can be seen from Figure S6 in the Supporting Information, the resulting uncertainty in F_{OTS} is ~ 80 pN. Furthermore, the uncertainty in A_{OTS} results from potential imperfections and packing density variations of the OTS monolayer. The A_{OTS} values of ~ 0.20,[26] 0.21,[28] or 0.43 nm^2 [27,55] (also see references therein) were derived from monolayers on flat surfaces, whereas the AFM tip presents a highly curved surface which could affect the self-assembly process. Even for the case of a flat substrate, imperfections and associated variations of the packing density of OTS monolayers were reported.[47,48] Bearing in mind these uncertainties in the absolute values of the adhesion force, F_{OTS}, between a single OTS molecule and graphene, it can be concluded that somewhat larger F_{OTS} values have been observed on 2LG domains relative to 1LG domains.

Although the values for F_{OTS} are relatively similar for 1LG to 2LG domains (Figure 6), they are still associated with distinct adhesion force contrasts (Figures 5a and 6a) and thus clearly observable under the chosen conditions. Following the rationale of Figure 1b, which applies to the present case of adhesion measurement in water, a highly polar liquid, this finding indicates that 1LG domains are less hydrophobic than 2LG domains.

CONCLUSIONS

A CFM-based approach has been demonstrated that allows differentiation of 1LG and 2LG domains with regard to their degree of hydrophobicity. Using hydrophobic AFM tips functionalized with CH_3-terminated silane molecules (OTS), spatial variations of the tip–sample adhesion force have been measured for the case of graphene samples grown epitaxially on SiC. In the presence of water, hydrophobic attraction occurs and a larger adhesion force has been measured on 2LG, as compared to 1LG domains, thus indicating that 2LG domains are more hydrophobic than 1LG domains. The contrast mechanism based on the hydrophobic attraction has also been demonstrated for the case of test samples exhibiting a hydrophobic/hydrophilic pattern. Thus, this approach involving CFM shows that variations in hydrophobicity occur between 1LG and 2LG. Conversely, under ambient conditions, an increased adhesion force was measured on 1LG, due to the prevailing capillary force resulting from the presence of a thin water layer.

Furthermore, by assuming Johnson–Kendall–Roberts contact mechanics and relating the measured adhesion force distributions to the tip–sample contact area, we calculated approximate values of ~ 300 and ~ 320 pN for the adhesion force between a single OTS molecule and 1LG and 2LG, respectively. Major sources of uncertainty are the tip size and the average surface area per molecule of the OTS monolayer on top of the highly curved AFM tip. Further to the adhesion force measurements, friction force measurements have shown a good sensitivity for spatial variations in the graphene surface chemistry. Hydrophobic domains with increased adhesion force were concurrently demonstrating a lower friction force. The friction contrast is consistent with the fact that different levels of hydrophobicity of 1LG and 2LG tend to affect the local arrangement of water molecules and, in turn, the sliding motion of the AFM tip. In addition, an increase in the tip–sample contact area and thus the measured friction force may result from out-of-plane puckering of 1LG domains.

In general, different levels of hydrophobicity cause variations in the wetting behavior under ambient conditions and are of particular relevance for applications where graphene devices or materials are exposed to nonzero levels of humidity. Measurement of domain-to-domain variations in the degree of hydrophobicity should allow detailed analysis of local doping effects and interfacial chemistry of graphene-based composites and nanosensors. Thus, the demonstrated method is a promising approach for the optimization of graphene devices operated under ambient conditions, as their characteristics and performance depend critically on the particulars of the graphene morphology and related variations in the propensity for water adsorption. Future studies could apply the approach demonstrated here to a range of graphene surfaces, with the aim to elucidate effects of the growth method or device fabrication technique on spatial variations in the degree of hydrophobicity, for example, to develop a better understanding of wetting behavior variations.

MATERIALS AND METHODS

Graphene Synthesis. The substrates (II−VI, Inc.) were $\sim 8 \times 8$ mm^2 in size and made of semi-insulating (0001)SiC (resistivity $> 10^{10}$ Ω cm), misoriented $\sim 0.05°$ from the basal plane mainly in the (11−20) direction. Graphene was synthesized *via* Si sublimation from SiC using an overpressure of an inert gas. Prior to synthesis, the substrates were etched in a H$_2$ atmosphere at 100 mbar using a temperature ramp from room

temperature to 1560 °C to remove polishing damage. At the end of the ramp, the H_2 was evacuated and Ar gas added to a pressure of 100 mbar (the transition takes about 2 min). The graphene was then synthesized at 1620 °C for 30 min in Ar. Afterward, the sample was cooled in Ar to 800 °C.[4] Two or more layers of graphene formed in this fashion are known to be Bernal stacked.[58]

Chemical Force Microscopy. Employing a Cypher AFM system (Asylum Research, Santa Barbara, CA), we measured the adhesion forces between chemically functionalized AFM probes and graphene surfaces. The AFM system was fitted with a superluminescent diode to minimize signal oscillations resulting from optical interference of a nonzero fraction of light reflected off the sample surface with the light reflected off the cantilever. The version of the Asylum Research control software was 111111+1719. The instrument was operated in a laboratory controlled to 22 ± 1 °C and 44 ± 10% relative humidity. It was calibrated using an NPL traceable blaze grating and a step height standard to ~6% relative uncertainty. The AFM cantilevers used were of type CSC38 with an aluminum reflective coating and a typical tip radius of ~8 nm (Mikromasch Europe, Germany). The optical lever sensitivity and the spring constant for cantilever deflection were measured by running force−displacement curves on a plain Si wafer surface and by recording spectra of the thermally excited cantilever vibrations, respectively. Of the three rectangular silicon cantilevers carried by a chip of type CSC38, cantilevers of ~300 or ~350 μm length were used with measured values of their spring constant in the range of ~80−200 and ~80−150 pN/nm, respectively. To allow hydrophobic behavior of the AFM tip, the cantilevers were functionalized with OTS. Prior to the immersion into a ~10^{-3} mol/L solution of OTS in toluene, the cantilevers were treated in a UV/ozone cleaner for ~20 min. Immediately after the immersion, the cantilevers were washed three times in chloroform, acetone, and again in chloroform. The AFM force measurements were undertaken in deionized water by immersing the cantilever into a drop of ~80 μL volume on top of the graphene sample. The force−displacement curves were run at a scan rate of ~0.81 Hz and a z-velocity of ~1.93 μm s^{-1}. They were recorded over an arrays of points, and the magnitude of the pull-off peaks occurring upon retraction of the probe was analyzed. Typically, the size of the resulting force maps was 64 × 64 pixels. To check the functionalization of the cantilevers and to characterize related adhesion contrasts, test samples with an array of Au squares on top of a Si/SiO_2 wafer surface were prepared. The array was fabricated using electron beam lithography (EBL) patterning of a resist layer, sputter coating, and subsequent lift-off. The Au squares measured ~1 × 1 μm^2 in size, and the thickness of the Au coating was ~70 nm on top of a ~7 nm thick NiCr adhesion layer. One of the two test samples was functionalized with OTS in the same way as the cantilevers. As the OTS molecules bind to the silica (SiO_2) surface of the Si wafer but not to the Au squares, the area between the hydrophilic Au squares is rendered hydrophobic. The second test sample was used with no further functionalization. After removal of carbonaceous contaminations by UV/ozone cleaning, the entire surface was rendered hydrophilic. Indeed, a drop of deionized water was found to wet the cleaned surface readily.

Kelvin Probe Force Microscopy under Ambient Conditions. Employing an Icon AFM system (Bruker Nano Surfaces, CA), pull-off forces and the electrical surface potential were measured in PeakForce mode, using highly doped Si probes (Bruker PFQNE-AL) with a spring constant of ~0.9 N/m. Measurements were carried out using the frequency-modulated KPFM (FM-KPFM) technique. The relative humidity in ambient conditions was ~40%.

Raman Spectroscopy. Raman intensity maps of the sample were obtained using a 2 mW 532 nm probe confocally focused by a 100× objective, resulting in a lateral spatial resolution of 0.4 ± 0.1 μm, and the scattered light was analyzed using a Horiba Jobin-Yvon HR800; the spectral resolution was 3.1 ± 0.4 cm^{-1}. The lateral spatial resolution has been determined by the first derivative of the Si 520 cm^{-1} band related Raman map of a Si calibration grating with a period of 3 μm.

Analysis of AFM Data. The initial processing of force map data was done using the microscope software, version 13.04.77 under IgorPro 6.34A. This part included setting of the calibration parameters and zeroing baseline offsets of force−indentation curves. For analysis of histograms the Scanning Probe Image Processor SPIP version 6.1.0 (Image Metrology, Denmark) was used. This step encompassed flattening and definition of masks to select certain areas, such as the gold squares of the test samples. Fitting of individual peaks of a distribution and calculation of the combined distribution were done using SigmaPlot version 12.0 (Systat Software, CA). The LFM images analyzed were calculated from the lateral force images measured in trace and retrace by $V_{lat} = (V_{lat}^{trace} - V_{lat}^{retrace})/2$.

Conflict of Interest: The authors declare no competing financial interest.

Supporting Information Available: Raman spectroscopy maps of epitaxial graphene synthesized on SiC, an adhesion map of test sample TS2 and its statistical analysis, statistical analysis of the adhesion map given in Figure 5a, line 143 of the lateral force image given in Figure 5d, and a plot illustrating the propagation of uncertainties in the tip radius R. The Supporting Information is available free of charge on the ACS Publications website at DOI: 10.1021/acsnano.5b03220.

REFERENCES AND NOTES

1. Novoselov, K. S.; Geim, A. K.; Morozov, S. V.; Jiang, D.; Zhang, Y.; Dubonos, S. V.; Grigorieva, I. V.; Firsov, A. A. Electric Field Effect in Atomically Thin Carbon Films. *Science* **2004**, *306*, 666–669.

2. Batzill, M. The Surface Science of Graphene: Metal Interfaces, CVD Synthesis, Nanoribbons, Chemical Modifications, and Defects. *Surf. Sci. Rep.* **2012**, *67*, 83–115.

3. Abergel, D. S. L.; Apalkov, V.; Berashevich, J.; Ziegler, K.; Chakraborty, T. Properties of Graphene: A Theoretical Perspective. *Adv. Phys.* **2010**, *59*, 261–482.

4. Nyakiti, L. O.; Wheeler, V. D.; Garces, N. Y.; Myers-Ward, R. L.; Eddy, C. R.; Gaskill, D. K. Enabling Graphene-Based Technologies: Toward Wafer-Scale Production of Epitaxial Graphene. *MRS Bull.* **2012**, *37*, 1149–1157.

5. Sato, Y.; Takai, K.; Enoki, T. Electrically Controlled Adsorption of Oxygen in Bilayer Graphene Devices (vol 11, Pg 3468, 2011). *Nano Lett.* **2011**, *11*, 3468–3475.

6. Sidorov, A. N.; Gaskill, K.; Buongiorno Nardelli, M.; Tedesco, J. L.; Myers-Ward, R. L.; Eddy, C. R.; Jayasekera, T.; Kim, K. W.; Jayasingha, R.; Sherehiy, A.; et al. Charge Transfer Equilibria in Ambient-Exposed Epitaxial Graphene on (0001) 6 H-SiC. *J. Appl. Phys.* **2012**, *111*, 113706.

7. Schedin, F.; Geim, A. K.; Morozov, S. V.; Hill, E. W.; Blake, P.; Katsnelson, M. I.; Novoselov, K. S. Detection of Individual Gas Molecules Adsorbed on Graphene. *Nat. Mater.* **2007**, *6*, 652–655.

8. Flueckiger, J.; Ko, F. K.; Cheung, K. C. Microfabricated Formaldehyde Gas Sensors. *Sensors* **2009**, *9*, 9196–9215.

9. Martinez-Martin, D.; Longuinhos, R.; Izquierdo, J. G.; Marele, A.; Alexandre, S. S.; Jaafar, M.; Gómez-Rodríguez, J. M.; Bañares, L.; Soler, J. M.; Gomez-Herrero, J. Atmospheric Contaminants on Graphitic Surfaces. *Carbon* **2013**, *61*, 33–39.

10. Kozbial, A.; Li, Z.; Sun, J.; Gong, X.; Zhou, F.; Wang, Y.; Xu, H.; Liu, H.; Li, L. Understanding the Intrinsic Water Wettability of Graphite. *Carbon* **2014**, *74*, 218–225.

11. Filleter, T.; Emtsev, K. V.; Seyller, T.; Bennewitz, R. Local Work Function Measurements of Epitaxial Graphene. *Appl. Phys. Lett.* **2008**, *93*, 133117.

12. Panchal, V.; Pearce, R.; Yakimova, R.; Tzalenchuk, A.; Kazakova, O. Standardization of Surface Potential Measurements of Graphene Domains. *Sci. Rep.* **2013**, *3*, 2597.

13. Rafiee, J.; Mi, X.; Gullapalli, H.; Thomas, A. V.; Yavari, F.; Shi, Y.; Ajayan, P. M.; Koratkar, N. A. Wetting Transparency of Graphene. *Nat. Mater.* **2012**, *11*, 217–222.

14. Li, Z.; Wang, Y.; Kozbial, A.; Shenoy, G.; Zhou, F.; McGinley, R.; Ireland, P.; Morganstein, B.; Kunkel, A.; Surwade, S. P.; et al. Effect of Airborne Contaminants on the Wettability of Supported Graphene and Graphite. *Nat. Mater.* **2013**, *12*, 925–931.

15. Kazakova, O.; Panchal, V.; Burnett, T. Epitaxial Graphene and Graphene–Based Devices Studied by Electrical Scanning Probe Microscopy. *Crystals* **2013**, *3*, 191–233.

16. Shih, C.-J.; Wang, Q. H.; Lin, S.; Park, K.-C.; Jin, Z.; Strano, M. S.; Blankschtein, D. Breakdown in the Wetting Transparency of Graphene. *Phys. Rev. Lett.* **2012**, *109*, 176101.

17. Taherian, F.; Marcon, V.; van der Vegt, N. F. A.; Leroy, F. What Is the Contact Angle of Water on Graphene? *Langmuir* **2013**, *29*, 1457–1465.

18. Lee, C.; Li, Q.; Kalb, W.; Liu, X.-Z.; Berger, H.; Carpick, R. W.; Hone, J. Frictional Characteristics of Atomically Thin Sheets. *Science* **2010**, *328*, 76–80.

19. Shim, J.; Lui, C. H.; Ko, T. Y.; Yu, Y.-J.; Kim, P.; Heinz, T. F.; Ryu, S. Water-Gated Charge Doping of Graphene Induced by Mica Substrates. *Nano Lett.* **2012**, *12*, 648–654.

20. Suk, M. E.; Aluru, N. R. Water Transport through Ultrathin Graphene. *J. Phys. Chem. Lett.* **2010**, *1*, 1590–1594.

21. Srivastava, N.; He, G.; Mende, P. C.; Feenstra, R. M.; Sun, Y. Graphene Formed on SiC under Various Environments: Comparison of Si-Face and C-Face. *J. Phys. D: Appl. Phys.* **2012**, *45*, 154001.

22. Hu, H.; Ruammaitree, A.; Nakahara, H.; Asaka, K.; Saito, Y. Few-Layer Epitaxial Graphene with Large Domains on C-Terminated 6H-SiC. *Surf. Interface Anal.* **2012**, *44*, 793–796.

23. Grodecki, K.; Bozek, R.; Strupinski, W.; Wysmolek, A.; Stepniewski, R.; Baranowski, J. M. Micro-Raman Spectroscopy of Graphene Grown on Stepped 4H-SiC (0001) Surface. *Appl. Phys. Lett.* **2012**, *100*, 261604.

24. Noy, A. Chemical Force Microscopy of Chemical and Biological Interactions. *Surf. Interface Anal.* **2006**, *38*, 1429–1441.

25. Clear, S.; Nealey, P. Chemical Force Microscopy Study of Adhesion and Friction between Surfaces Functionalized with Self-Assembled Monolayers and Immersed in Solvents. *J. Colloid Interface Sci.* **1999**, *213*, 238–250.

26. Van der Vegte, E. W.; Hadziioannou, G. Scanning Force Microscopy with Chemical Specificity: An Extensive Study of Chemically Specific Tip–Surface Interactions and the Chemical Imaging of Surface Functional Groups. *Langmuir* **1997**, *13*, 4357–4368.

27. Ito, T.; Namba, M.; Bühlmann, P.; Umezawa, Y. Modification of Silicon Nitride Tips with Trichlorosilane Self-Assembled Monolayers (SAMs) for Chemical Force Microscopy. *Langmuir* **1997**, *13*, 4323–4332.

28. Beake, B. D.; Leggett, G. J. Friction and Adhesion of Mixed Self-Assembled Monolayers Studied by Chemical Force Microscopy. *Phys. Chem. Chem. Phys.* **1999**, *1*, 3345–3350.

29. Munz, M.; Mills, T. Size Dependence of Shape and Stiffness of Single Sessile Oil Nanodroplets as Measured by Atomic Force Microscopy. *Langmuir* **2014**, *30*, 4243–4252.

30. Robinson, B. J.; Kay, N. D.; Kolosov, O. V. Nanoscale Interfacial Interactions of Graphene with Polar and Nonpolar Liquids. *Langmuir* **2013**, *29*, 7735–7742.

31. Ding, Y.-H.; Zhang, P.; Ren, H.-M.; Zhuo, Q.; Yang, Z.-M.; Jiang, X.; Jiang, Y. Surface Adhesion Properties of Graphene and Graphene Oxide Studied by Colloid-Probe Atomic Force Microscopy. *Appl. Surf. Sci.* **2011**, *258*, 1077–1081.

32. Lee, H.; Lee, N.; Seo, Y.; Eom, J.; Lee, S. Comparison of Frictional Forces on Graphene and Graphite. *Nanotechnology* **2009**, *20*, 325701.

33. Farshchi-Tabrizi, M.; Kappl, M.; Cheng, Y.; Gutmann, J.; Butt, H.-J. On the Adhesion between Fine Particles and Nanocontacts: An Atomic Force Microscope Study. *Langmuir* **2006**, *22*, 2171–2184.

34. Xiao, X.; Qian, L. Investigation of Humidity-Dependent Capillary Force. *Langmuir* **2000**, *16*, 8153–8158.

35. Jones, R.; Pollock, H. M.; Cleaver, J. A. S.; Hodges, C. S. Adhesion Forces between Glass and Silicon Surfaces in Air Studied by AFM: Effects of Relative Humidity, Particle Size, Roughness, and Surface Treatment. *Langmuir* **2002**, *18*, 8045–8055.

36. Chen, L.; Gu, X.; Fasolka, M. J.; Martin, J. W.; Nguyen, T. Effects of Humidity and Sample Surface Free Energy on AFM Probe-Sample Interactions and Lateral Force Microscopy Image Contrast. *Langmuir* **2009**, *25*, 3494–3503.

37. Knapp, H.; Stemmer, A. Preparation, Comparison and Performance of Hydrophobic AFM Tips. *Surf. Interface Anal.* **1999**, *27*, 324–331.

38. Gourianova, S.; Willenbacher, N.; Kutschera, M. Chemical Force Microscopy Study of Adhesive Properties of Polypropylene Films: Influence of Surface Polarity and Medium. *Langmuir* **2005**, *21*, 5429–5438.

39. Butt, H.-J.; Cappella, B.; Kappl, M. Force Measurements with the Atomic Force Microscope: Technique, Interpretation and Applications. *Surf. Sci. Rep.* **2005**, *59*, 1–152.

40. Kokkoli, E.; Zukoski, C. Effect of Solvents on Interactions between Hydrophobic Self-Assembled Monolayers. *J. Colloid Interface Sci.* **1999**, *209*, 60–65.

41. Tyrrell, J. W. G.; Attard, P. Images of Nanobubbles on Hydrophobic Surfaces and Their Interactions. *Phys. Rev. Lett.* **2001**, *87*, 176104.

42. Li, Z.; Yoon, R.-H. Thermodynamics of Hydrophobic Interaction between Silica Surfaces Coated with Octadecyltrichlorosilane. *J. Colloid Interface Sci.* **2013**, *392*, 369–375.

43. Mishchuk, N. A. The Model of Hydrophobic Attraction in the Framework of Classical DLVO Forces. *Adv. Colloid Interface Sci.* **2011**, *168*, 149–166.

44. Ryu, S.; Liu, L.; Berciaud, S.; Yu, Y.-J.; Liu, H.; Kim, P.; Flynn, G. W.; Brus, L. E. Atmospheric Oxygen Binding and Hole Doping in Deformed Graphene on a SiO2 Substrate. *Nano Lett.* **2010**, *10*, 4944–4951.

45. Yu, Y.-J.; Zhao, Y.; Ryu, S.; Brus, L. E.; Kim, K. S.; Kim, P. Tuning the Graphene Work Function by Electric Field Effect. *Nano Lett.* **2009**, *9*, 3430–3434.

46. Kim, J.-H.; Hwang, J. H.; Suh, J.; Tongay, S.; Kwon, S.; Hwang, C. C.; Wu, J.; Young Park, J. Work Function Engineering of Single Layer Graphene by Irradiation-Induced Defects. *Appl. Phys. Lett.* **2013**, *103*, 171604.

47. Choi, S.-H.; Zhang Newby, B. Alternative Method for Determining Surface Energy by Utilizing Polymer Thin Film Dewetting. *Langmuir* **2003**, *19*, 1419–1428.

48. Flater, E. E.; Ashurst, W. R.; Carpick, R. W. Nanotribology of Octadecyltrichlorosilane Monolayers and Silicon: Self-Mated *versus* Unmated Interfaces and Local Packing Density Effects. *Langmuir* **2007**, *23*, 9242–9252.

49. Maccarini, M.; Himmelhaus, M.; Stoycheva, S.; Grunze, M. Characterisation and Stability of Hydrophobic Surfaces in Water. *Appl. Surf. Sci.* **2005**, *252*, 1941–1946.

50. Vezenov, D. V.; Noy, A.; Lieber, C. M. The Effect of Liquid-Induced Adhesion Changes on the Interfacial Shear Strength between Self-Assembled Monolayers. *J. Adhes. Sci. Technol.* **2003**, *17*, 1385–1401.

51. Bowden, F.; Tabor, D. *The Friction and Adhesion of Solids—Part 2*; Clarendon Press: Oxford, U.K., 1964.

52. Baudry, J.; Charlaix, E.; Tonck, A.; Mazuyer, D. Experimental Evidence for a Large Slip Effect at a Nonwetting Fluid–Solid Interface. *Langmuir* **2001**, *17*, 5232–5236.

53. Poynor, A.; Hong, L.; Robinson, I.; Granick, S.; Zhang, Z.; Fenter, P. How Water Meets a Hydrophobic Surface. *Phys. Rev. Lett.* **2006**, *97*, 266101.

54. Maugis, D. *Contact, Adhesion and Rupture of Elastic Solids*; Springer: Berlin, 2000; p 415.

55. Fujii, M.; Sugisawa, S.; Fukada, K.; Kato, T.; Shirakawa, T.; Seimiya, T. Packing of Hydrocarbon and Perfluorocarbon Chains Planted on Oxidized Surface of Silicon As Studied by Ellipsometry and Atomic Force Microscopy. *Langmuir* **1994**, *10*, 984–987.

56. Lee, C.; Wei, X.; Kysar, J. W.; Hone, J. Measurement of the Elastic Properties and Intrinsic Strength of Monolayer Graphene. *Science* **2008**, *321*, 385–388.
57. Kudin, K.; Scuseria, G.; Yakobson, B. C2F, BN, and C Nanoshell Elasticity from Ab Initio Computations. *Phys. Rev. B: Condens. Matter Mater. Phys.* **2001**, *64*, 235406.
58. Ohta, T.; Bostwick, A.; McChesney, J.; Seyller, T.; Horn, K.; Rotenberg, E. Interlayer Interaction and Electronic Screening in Multilayer Graphene Investigated with Angle-Resolved Photoemission Spectroscopy. *Phys. Rev. Lett.* **2007**, *98*, 206802.